

LETTER TO THE EDITOR

Perturbative reconstruction of a gravitational lens: when mass does not follow light

C. Alard¹

Institut d'Astrophysique de Paris, 98bis boulevard Arago, 75014 Paris
e-mail: alard@iap.fr

ABSTRACT

Aims. The structure and potential of a complex gravitational lens is reconstructed. This lens is composed of 6 galaxies belonging to a small group.

Methods. The lens inversion is reduced to the problem of reconstructing non-degenerate quantities: the 2 fields of the perturbative theory of strong gravitational lenses. Since in the perturbative theory the circular source solution is analytical, the general properties of the perturbative solution can be inferred directly from the data. As a consequence, there is no degeneracy in the reconstruction of the perturbative fields, finding the best solution is only a matter of numerical refinement.

Results. The local shape of the potential and density of the lens are inferred from the perturbative solution, revealing the existence of an independent dark component that does not follow light.

Conclusions. The most likely explanation is that the particular shape of the dark halo is due to the merging of dark matter halo's. This is a unique and new result illustrating the structure of the dark halo's at the scale of galaxies.

Key words. gravitational lensing - cosmology:dark matter

1. Introduction.

The multiple images of a distant source formed by a gravitational lens constrain the value of the lens potential at the images locations. Additional constraints comes from the fact that no images are formed in dark areas (Diego *et al.* 2005). However, since there are no constraints on the potential in other areas, the problem is degenerate, and an infinite number of models are possible. In this context, the newly developed perturbative theory of strong gravitational lenses (Alard 2007) has the advantage to describe the lens using fundamental physical quantities and not degenerate potential models. In the perturbative theory of order 1, the lens is represented by 2 angular functionals which are the 2 perturbative fields (see Alard 2007, Eq's 5,6,7 and 8). These fields have physical meaning: the first field f_1 represents the mean radial position of the image, while the second field $\frac{df_0}{d\theta}$ controls image formation and is directly related to the image radial size (see Alard 2007, Eq. 12). Extensive numerical experiments shows that the order 1 perturbative theory is an



Fig. 1. Color image for SL2SJ021408-053532 reconstructed from 3 noise filtered HST images in 3 bands.

effective and accurate description of realistic CDM halo's lens models (Peirani *et al.* 2008). Consequently the inversion problem is reduced to the estimation of these 2 perturbative fields. The reduction of the degeneracy problem in this approach is well illustrated by the fact that an infinite number of models corresponds to a given perturbative representation. The concepts developed in this approach are very different from some recent perturbative numerical schemes (see for instance Vegetti & Koopmans 2009). In this type of work there are no attempt at reformulating the lens-inversion problem in terms of fundamental quantities, the main goal is to derive an efficient numerical scheme to solve the ordinary lens-equation.

2. The data.

The gravitational lens SL2SJ021408-053532 (Cabanac *etal.* 2007, SL2S public domain) was observed by HST in 3 spectral domain, F475W, F606W, F814W, with an exposure time of 400 sec. Cosmics cleaning and image re-interpolation to a common grid are performed using software's from the ISIS package (Alard 2000). These 3 images are stacked, and the background is subtracted to produce a reference image of the arc system. A color illustration of the arc system is also provided in Fig (1).

3. Fields reconstruction.

3.1. Basic equations

The basic equations of the perturbative theory will be reminded in this section, for more details, see Alard (2007), and in particular, Eq's (5,6,7 and 8). Considering a circular

background $\phi_0(r)$, and a perturbation $\psi(r, \theta)$, the potential $\phi(r, \theta)$ reads:

$$\begin{cases} \phi(r, \theta) &= \phi_0(r) + \epsilon\psi(r, \theta) & \epsilon \ll 1 \\ \psi(r, \theta) &= f_0(\theta) + f_1(\theta)(r - 1) \\ f_n(\theta) &= \frac{1}{n!} \left[\frac{\partial^n \psi}{\partial r^n} \right]_{(r=1)} \end{cases} \quad (1)$$

Which leads to the perturbative lens equation:

$$\begin{cases} \mathbf{r}_s = (\kappa_2 dr - f_1) \mathbf{u}_r - \frac{\partial f_0}{\partial \theta} \mathbf{u}_\theta \\ \kappa_2 = 1 - \left[\frac{d^2 \phi_0}{dr^2} \right]_{(r=1)} \end{cases} \quad (2)$$

Note that Eq. (2) depends on κ_2 , however this variable can be eliminated by re-normalizing the fields: $f_n = \frac{f_n}{\kappa_2}$, and the source plane coordinates, $\mathbf{r}_s = \frac{\mathbf{r}_s}{\kappa_2}$ (mass sheet degeneracy). These re-normalized variables will be adopted in the continuation of this work. Note also that in the same spirit as Eq. (10) in Alard (2007) the impact parameters will be included in the fields, and the source will be re-centered, by making the following change in variables:

$$\begin{cases} \tilde{\mathbf{r}}_s = \mathbf{r}_s - \mathbf{r}_0 \\ \tilde{f}_i = f_i + x_0 \cos \theta + y_0 \sin \theta & i = 0, 1 \end{cases} \quad (3)$$

3.2. Local field re-construction.

The reconstruction of the 2 perturbative fields by local linear method is explained in details in Alard (2008), see in particular Sec. 3.3. The basic idea in this method is to describe the local field at the scale of the images by local polynomial approximations. An initial guess for the local polynomials can be obtained by considering the circular source solution. This guess is refined by non-linear maximization of the cross-correlation of the images in the source plane. This method is applied to the system of 4 images formed by the lens. The first 2 images are situated in the large arc in the upper left (they appear as 2 identical mirror images), while the 2 other images, are at the bottom and the right side of the frame (see 1). The images are small enough to try a local linear model. The best local linear model result in a mean cross-correlation of $\simeq 0.8$ between the images which is a good indication the linear approximation is appropriate, see Fig. (2) for an illustration.

3.3. Refining the solution.

The local linear solution obtained in the former section is already an excellent approximate of the solution. However, it is still possible to improve a little this solution, first by taking into account the image convolution with the PSF, and second by considering field model beyond the local linear approximation. To take into account the PSF convolution it is necessary to implement an iterative method: start from the solution estimated in Sec (3.2), reconstruct the source and its system of images, convolve with the PSF and compare to the HST data by chi-square estimation. Note that this chi-square can be interpreted as a

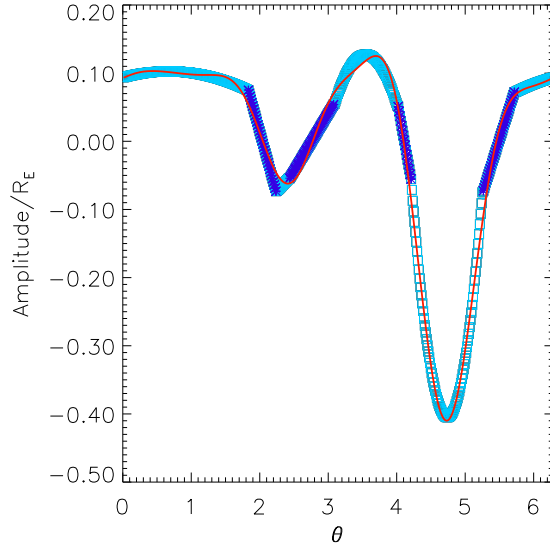


Fig. 2. The guess for the $\frac{df_0}{d\theta}$ field. The blue line segments represents the local linear guess at the image location, while the light blue curves are the second order interpolations between images. The red line is an adjustment of a 6th order Fourier serie to the blue curve.

comparison between the images. All images come from the same source, thus the chi-square measure directly the image similarity in the lens plane.

3.3.1. Source reconstruction

At this point the simplest method to estimate the source would be to use Warren & Dye (2003) method. Unfortunately the source is very complex, and this method would require using too many basis functions. The following method has been preferred: images are co-added in the source plane using an algorithm that preserve the geometrical properties of the images elements. The drawback in this method is that the images pixels are affected by the convolution with the PSF, and thus the source reconstruction is not as perfect as it should be. However, it is easy to correct this effect by the using the following procedure: first ignore the effect of the PSF on source reconstruction, find a solution, and then correct the effect using a deconvolution procedure very similar to the Van-Cittert method. The basic idea in this de-convolution of the source is to consider the residual between the image and model, take it as a new input, find a correction to the source, and iterate. This process converges quickly and provide quite significant corrections in bright areas, and almost no correction in other areas.

3.3.2. More refined field models

There are 2 steps in refining the field model, first the local model can be extended to the full angular range. The gaps between the images are filled by using second order polynomials, with the constraint that no images are formed in dark areas Diego *et al.* (2005), that the sum of the field $\frac{df_0}{d\theta}$ is zero, and that the field must be as smooth as possible. The first

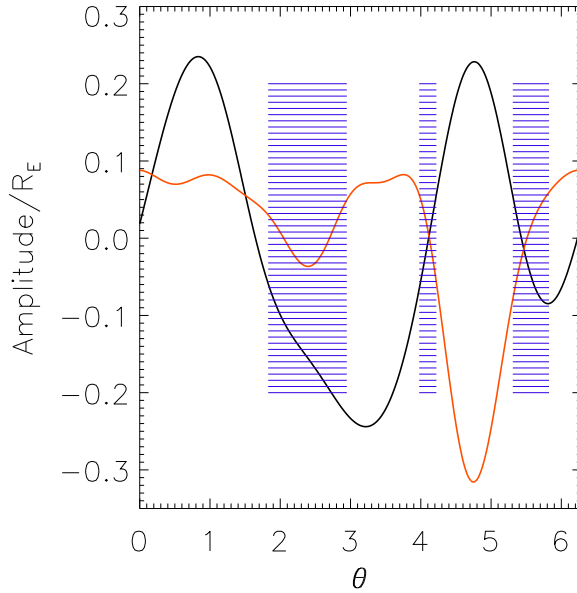


Fig. 3. Best solution for the fields: red curve, $\frac{d\tilde{f}_0}{d\theta}$, and black curve \tilde{f}_1 . The blue dashes indicates areas where images are present.

constraint implies that the field is larger in dark areas than in light areas, while the second constraint reduces the number of free parameters. The numerical solution is presented in Fig. (2). The second step is to approximate the polynomial solution by a Fourier expansion of order 6. Note that using Fourier expansion is not essential in this method, and that it would have been possible to continue with spline polynomial models, but since the Fourier expansion is related to the multipole expansion of the potential (Alard 2008, Eq. 13), it is more convenient to express the result using this familiar model.

3.3.3. Final fitting of the fields.

Using the former methods to reconstruct the source and the fields, the best solution is found by non-linear optimization of the chi-square using the simplex method (Nelder & Mead, 1965). The final solution, the source reconstruction and the image re-construction are presented in Fig. (4), while the field solution is presented in Fig. (3).

3.4. Noise.

The model and the data are compared in a region around the arcs with total number of pixels N . The Poisson weighted difference R_i between the model at pixel i , M_i and the HST data D_i is very close to a Gaussian . The relevant chi-square, considering that the model has N_P parameters (including the source parameters) is $\chi_{2/dof}^2 = \frac{1}{N-N_P} \sum_i R_i^2 \simeq 1.17$ which confirms the good quality of the fit. The corresponding noise on the estimation of the Fourier coefficients is evaluated by local linearization methods near the minima (See Press *et al.* (2007)) This analysis shows that the errors on the Fourier coefficients due to the Poisson noise are $\simeq 10^{-3}$, which is quite small. Considering that the error due to the perturbative approximation σ_{Pert} is of order 1% (Peirani *et al.* 2008), and that the relevant

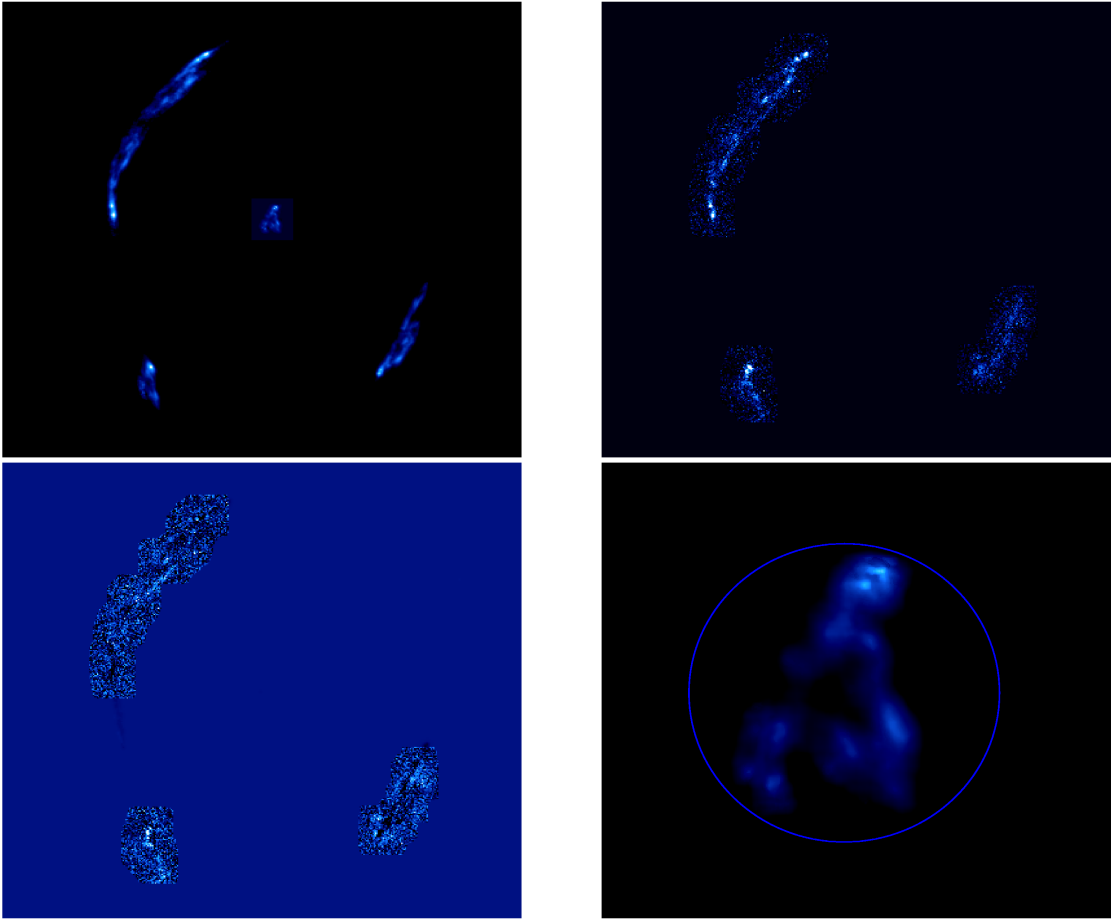


Fig. 4. Results from image re-construction: HST data (upper right), model (upper left), data/model subtraction (lower left), source (lower-right). Note the reproduction of the source details in the images of the model. The repetition of conjugate points is especially well visible between the 2 nearby images of the source situated in the upper left of the image. An image of the source has been super-imposed to the model (upper left), to illustrate the scaling.

error on the fields is similar, the noise in reconstructing the potential will be dominated by $\sigma_{Pert} \simeq 0.01$.

4. Prediction of images colors.

Figure (5) indicates that last image (lower right position in Fig. (1)) does not have the typical "hat-shaped" color diagram observed for the 3 other images. But this feature is actually a prediction of the perturbative model. The first half of the light in the last image comes from the same source area as the other images, but the remaining light comes from an area of the source that has no counterparts in the large arcs, and only a tiny counterpart in the lower left image. This situation is due to the crossing of the caustic line by a faint part of the source which is visible in Fig. 5 at the lower left of source-caustic diagram. As a consequence, the first half of the last image should have the same color diagram as the other images, and this exactly what is observed (see Fig. 5). The remaining part should have the same color as the faint parts of the source, and this is also what Fig. (5)

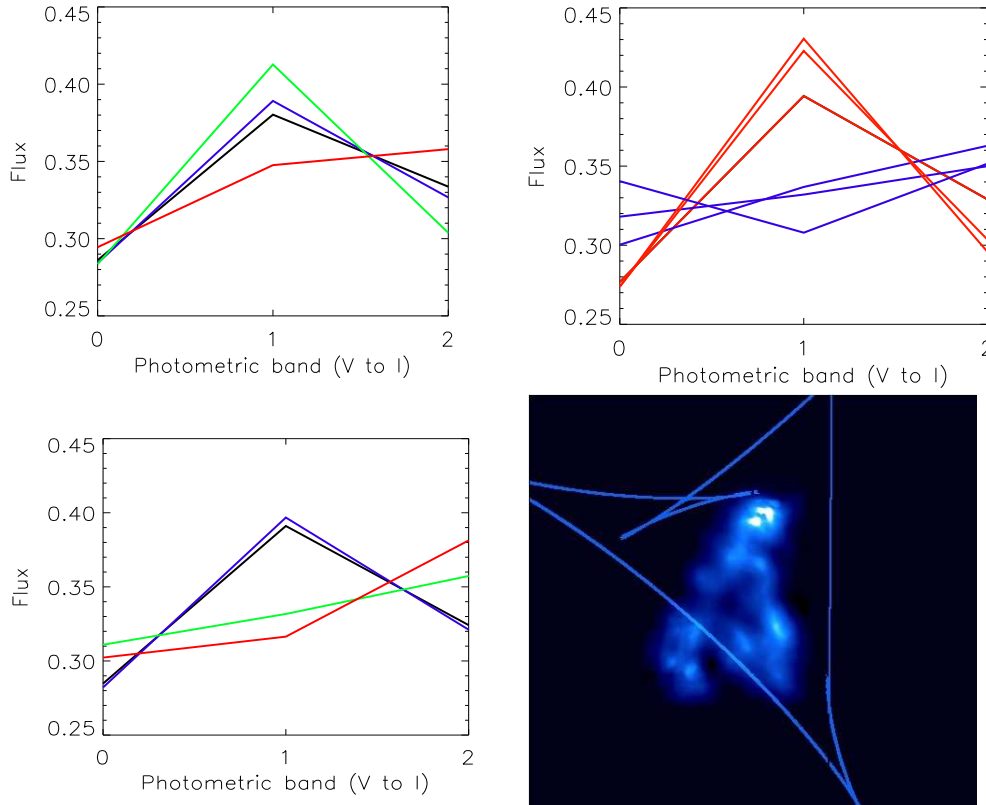


Fig. 5. This figure presents the 3 color diagrams, obtained by taking the sequence of raw flux in the 3 HST bands, as well, as the source-caustic system (lower right). The plot on the upper left presents the color the last image (red), and of the 3 other images. The upper right plot presents the color diagram for the bright parts of the first 3 images (red curves), while the blue curves represents the faint parts of the source. The lower right plot, compares the color diagram of the first half of the last image (black curve), to the mean diagram of the 3 other images (blue curve), and also compares the color diagram of the second half of the last image (green curve), to the mean color diagram of faint source parts in the 3 other images (red curve).

illustrates. The color variations in the source are entirely related to the different colors of the small bright parts as illustrated in (5), it shows also that these bright spots even if not very well visible in the last image have to be there. The explanation of the observed colors of the images is a nice confirmation of the model.

5. Shape of the dark component.

The potential estimation follows directly from the field estimation (Eq. 1). In particular, calculations to first order shows that the local potential iso-contour near the critical circle r_ϕ is related to f_0 :

$$r_\phi = 1 - f_0(\theta) \quad (4)$$

However in practice only \tilde{f}_0 is known, and Eq. (3) shows that the first order coefficients of \tilde{f}_0 depends also on the impact parameters. But these first order terms are related to

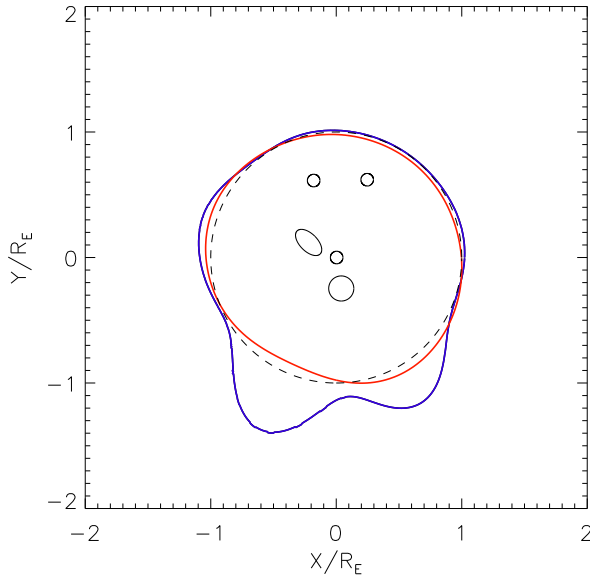


Fig. 6. The potential iso-contour: $dr = -\tilde{f}_0$ (red curve), and the unit circle (dashed line). The distance between the blue curve and the unit circle is proportional to the deviation from circularity. The small black contours represents the galaxies.

the centering of the potential, not to its shape, for instance the ellipticity is related to order 2 Fourier terms. It is however possible to obtain some partial information about the centering of the potential by using Eq. (13) in Alard (2008), the first order moments within the unit circle do not depend on the impact parameters, they are quite small, of the order of $0.1R_E$. The outer moments have to be of the same order, and thus the centering terms are not large. Note that equations have been normalized by the factor κ_2 and that κ_2 acts as an unknown scaling factor on the potential iso-contours. However, it is important to note that this scaling degeneracy does not affect the shape of the potential, and that for realistic halo's κ_2 is close to unity (Peirani *et al.* 2008). The potential iso-contours $dr = -\tilde{f}_0$ presented in Fig. 6 shows that the maximum deviation from circularity are not consistent with the galaxies positions, which demonstrates that mass does not follow light in this system. Note also that Eq. (13) in Alard (2008) relates the fields Fourier coefficients to the inner and outer terms of the multipole expansion. As a consequence it is possible to show that the reconstruction is dominated by the inner terms, which clearly rules out an outer perturber as the source of the observed effects. To go further than the potential estimation it is necessary to make some assumptions. Since CDM halo's have nearly isothermal slopes in large domains, it is reasonable to assume a nearly isothermal background potential $\phi_0(r) \propto r^{1+\epsilon d_\alpha}$, which leads to:

$$\phi(r, \theta) = r + \epsilon r d_\alpha (\log(r) - 1) + \epsilon (f_0(\theta) + f_1(\theta)(r - 1)) \quad (5)$$

The density near the critical circle can be estimated by using Eq. (5) and the Poisson equation:

$$\rho(r, \theta) = 1 + \epsilon \left(d_\alpha - dr + f_1(\theta) + \frac{d^2 f_0}{d\theta^2} \right) \quad (6)$$

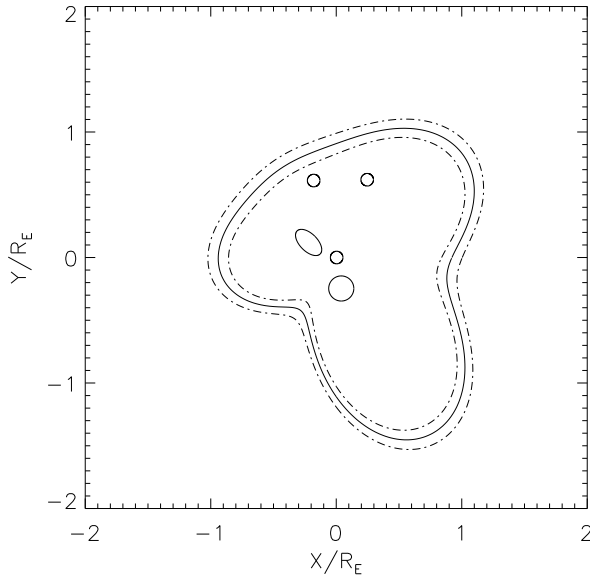


Fig. 7. Estimation of the projected density iso-contour near the critical radius. The dashed lines are the 3σ envelopes estimated assuming 1% noise on the reconstruction of f_1 , and $\frac{df_0}{d\theta}$

From Eq. (6) it is straightforward to derive the position of the perturbed iso-contour:

$$dr = f_1(\theta) + \frac{d^2 f_0}{d\theta^2} \quad (7)$$

Note that in Eq. (7) the terms corresponding to the impact parameters cancels out, and that κ_2 disappear in the nearly isothermal expansion. To maximize signal to noise the iso-contours presented in Fig. (7) are reconstructed by using an order 4 Fourier expansion. Note that a method to reconstruct the iso-contours of nearly isothermal lens density was also studied by Evans & Witt (2003). However their description of the potential is less general since it contains only one angular functional, it is suited only for potentials with constant iso-contours. The shape of the contours suggests that lens may be approximated by 2 ellipsoids. A decent fit of the arcs system could be obtained using such lens models. The images obtained by ray-tracing, for the 2 ellipsoids solution were compared to the perturbative approximation, a very good agreement was found, which is a validation of the perturbative approximation for this lens.

6. Discussion.

This paper reveals the structure of the dark matter envelope of a small group of galaxies, and shows that it does not follow light. The mass scale investigated is much below the the mass of the bullet cluster (Clowe *et al.* 2006). This small group is much simpler than a cluster and the interpretation of the results are not ambiguous, we are probably observing the merging of cold dark matter halo's. As a conclusion, the combination of the perturbative method and good HST data is clearly opening new possibilities in the exploration of the dark matter structure at the mass scale of galaxies.

Acknowledgements. This work is based on HST data, credited to STScI and prepared for NASA under Contract NAS 5-26555.

References

- Alard, C., 2000, A&AS, 144, 363
Alard, C., 2007, MNRAS Letters, 382, 58
Alard, C., 2008, MNRAS, 388, 375
Cabanac, R., & 15 authors, 2007, A&A, 461, 813
Clowe, D., Brada, M., Gonzalez, A., Markevitch, M., Randall, S., Jones, C., Zaritsky, D., ApJ, 648L, 10
Diego, J.M., Protopapas, P., Sandvik, H.B., Tegmark, M., 2005, MNRAS, 360, 477
Evans, N., Witt, H., 2003, MNRAS, 345, 1351
Krist, J., 1995, ASPC, 77, 349
Nelder, J., Mead, R., 1965, Computer Journal, 7, 308
Press, W., Teukolsky, S., Vetterling, W., Flannery, B., Numerical Recipes, Cambridge University Press, 2007
Peirani, S., Alard, C., Pichon, C., Gavazzi, R., Aubert, D., 2008, MNRAS, 390, 945
Vegetti, S., Koopmans, L., 2009, MNRAS, 392, 945
Warren, S., Dye, S., 2003, ApJ, 590, 673